# Landau-level-dependent photonic spin Hall effect in monolayer WTe<sub>2</sub>

Qiaoyun Ma,<sup>1</sup> Hui Dou,<sup>1</sup> Yiting Chen,<sup>2</sup> Guangyi Jia,<sup>1,\*</sup> Xinxing Zhou<sup>2,3,4,†</sup>

<sup>1</sup>School of Science, Tianjin University of Commerce, Tianjin 300134, P.R. China

<sup>2</sup>Key Laboratory of Low-Dimensional Quantum Structures and Quantum Control of Ministry of Education, School of Physics and Electronics, Hunan Normal University, Changsha 410081, P.R. China

<sup>3</sup>Key Laboratory of Physics and Devices in Post-Moore Era, College of Hunan Province, Changsha 410081, P.R. China

<sup>4</sup>Institute of Interdisciplinary Studies, Hunan Normal University, Changsha 410081, P.R. China

<sup>\*</sup>gyjia87@163.com; †xinxingzhou@hunnu.edu.cn

Landau level (LL) engineered photonic spin Hall effect (PSHE) holds great promise for nanoscale manipulation and steering of magneto-optical transport in two-dimensional atomic systems. Herein, we theoretically investigate PSHE modulated by LL transitions  $\delta n = n' - n = 0$ ,  $\pm 2$  (where n and n' indicate the LL indexes of valence and conduction bands, respectively) in monolayer WTe<sub>2</sub>. Results show that PSHE tuned by  $\delta n = 0, \pm 2$  has completely different dependent behaviors on LLs, incident angle of incident photons, and magnetic induction intensity. These discrepancies are ascribed to Hall-conductivity-incurred Hall angle  $\Theta$  because the variation tendency of photonic spin Hall shifts is similar to that of  $\Theta$  with changing the LL index. Giant PSHE with the largest in-plane displacement of more than 400 times of incident wavelength is obtained at the transition  $|n=55\rangle \rightarrow |n'=57\rangle$ . Remarkably enhanced PSHE occurs at near-zero Hall angles. Inplane and transverse spin-dependent displacements give their respective extremum values at the same incident angles when the  $\Theta$  is near to zero, and their incident-angle deviation will become larger and larger as the  $|\Theta|$  increases. This unambiguously confirms the strong influence of Hall angle in the PSHE, shedding important insights into the fundamental properties of spin-orbit interaction of light in time-reversal symmetry breaking quantum systems.

#### I. INTRODUCTION

The response of two-dimensional (2D) electron gases to an external magnetic field empowers 2D materials with many intriguing magneto-optical transport merits [1,2]. One of the most representative merits is the transformation of continuous electronic energy band into a series of discrete Landau levels (LLs). LLs are cornerstones of the quantum Hall effect, where the quantization of Hall conductance is directly related to the filling of LLs. And the energy separation between adjacent LLs is determined by the magnetic field strength and LL index. Furthermore, band parameters including the Fermi velocity and the effective mass of charge carriers are retrievable from the experimentally acquired LL spectrum [3,4]. This analytical approach has already demonstrated its effectiveness in characterizing a range of materials, such as graphene, black

phosphorus, and topological metals, etc [4-8]. By virtue of these admirable properties, LL splitting opens up new avenues in the manipulation of photonic spin Hall effect (PSHE), which can not only quantizedly enhance the spin splitting magnitude of photons but also realize precise tuning of the PSHE response via external magnetic field modulation-allowing dynamic control over the spin-dependent lateral shift of light beams without altering material's self-structure [9-11].

PSHE is generally accepted as a result of an effective spin-orbit interaction, which describes the mutual influence of the spin (polarization) and trajectory of light beam [12,13]. It is also regarded as a direct photonic analog of the electronic spin Hall effect, in which the electron spin and electric potential gradient are substituted by the optical helicity of incident photons and the refractive index

gradient, respectively. In conventional optical processes, PSHE occurs at the sub-wavelength scale due to the inherent weak spin-orbit interaction. In recent years, researchers have attempted to enhance the PSHE by imposing a tunable magnetic field [9-11], and the synergistic combination of matter magnetization and PSHE manipulation has shown great promise for cutting-edge applications including barcode encryption [11], probing quantum geometric capacitance [14], and sensing deepsubwavelength disorders in materials [15], and so forth. Magnetic-field-modulated PSHE has been studies in many materials, however, most of them rely on intrinsic magnetic ordering or magnetic dopants to induce magneto-optical responses and do not involve LLs [13-17]. To our knowledge, LL-engineered PSHE has been only reported in graphene, black phosphorus, and topological silicene thus far [9-11,18,19]. More unfortunately, these scarce studies are mainly focused on superficial quantization phenomenon-with little attention paid to the variation of Hall angle induced by LL transitions-and lack systematic investigations on the correlation between LL index, Hall angle evolution, and photonic spin splitting [9-11,18,19]. The in-depth regulatory mechanism of PSHE by different LL transitions remains ambiguous.

In the present work, we perform a theoretical study on LL-dependent PSHE in anisotropic monolayer WTe<sub>2</sub>. The model based on an effective  $k \cdot p$  Hamiltonian and linear-response theory is built to get LL spectra and magneto-optical conductivity tensor of WTe<sub>2</sub> for PSHE analyses. We explore how LL transitions  $\delta n = 0$ ,  $\pm 2$ , LL index n ranging from 1 to 61, and LL-dependent Hall angle impact in-plane and transverse photonic spin Hall shifts. Results show that giant spin Hall shifts, hundreds of times of the incident wavelength, can be obtained at appropriate LL transitions. The possible regulatory mechanism is discussed in detail.

# II. MODEL AND THEORETICAL METHODS

In monolayer 1T'-WTe<sub>2</sub>, the valence band mainly consists of *d*-orbitals of W atom, while the conduction band mainly consists of  $p_{\gamma}$ -orbitals of Te atom. Its low

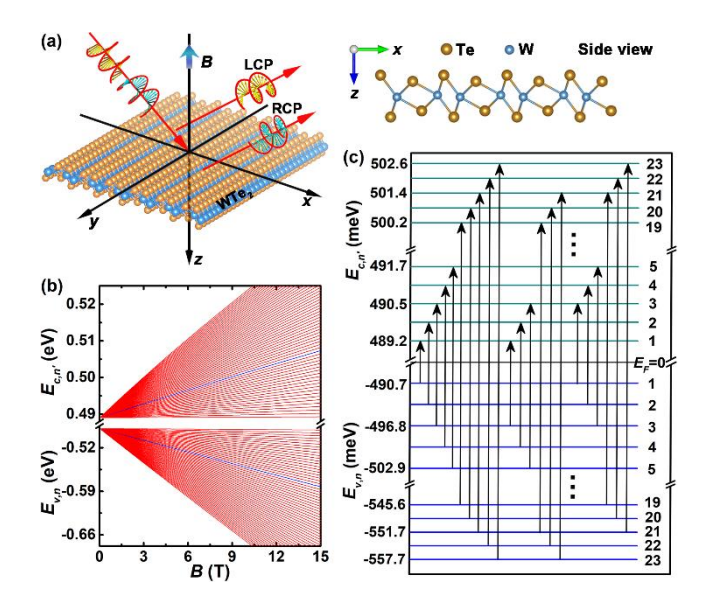


FIG. 1. (a) Schematic diagram of the photonic spin splitting of one Gaussian beam reflected from free-suspended monolayer WTe<sub>2</sub>. An imposed static magnetic field B is applied along the negative z axis in a Cartesian coordinate system. Upper right subgraph: side view of the crystallographic structure of WTe<sub>2</sub>. (b) LLs of conduction and valence bands of monolayer WTe<sub>2</sub> in different magnetic fields. LLs at n = n' = 21 are marked by blue lines. The number of basis function used in the calculation is 200 to get convergent numerical results. (c) Schematic illustration of the interband transition rules at B = 10T, where numbers on right side indicate LL indexes (LLs  $6 \le n(n') \le 18$  are not sketched and are implied by ellipses).

energy  $k \cdot p$  Hamiltonian can be expressed as [20-22]

$$H_{k \cdot p} = \begin{pmatrix} E_{c}(k_{x}, k_{y}) & 0 & -i\gamma_{1}k_{x} & \gamma_{2}k_{y} \\ 0 & E_{c}(k_{x}, k_{y}) & \gamma_{2}k_{y} & -i\gamma_{1}k_{x} \\ i\gamma_{1}k_{x} & \gamma_{2}k_{y} & E_{v}(k_{x}, k_{y}) & 0 \\ \gamma_{2}k_{y} & i\gamma_{1}k_{x} & 0 & E_{v}(k_{x}, k_{y}) \end{pmatrix}, \tag{1}$$

where  $E_c\left(k_x,k_y\right) = -\Delta - \alpha k_x^2 - \beta k_y^2$  and  $E_v\left(k_x,k_y\right) = \Delta + \lambda k_x^2 + \eta k_y^2$  are the on-site energies of p and d orbitals in WTe<sub>2</sub>, respectively, with  $\Delta = -0.489$  eV representing the d-p band inversion at  $\Gamma$  point in the Brillouin zone. The factors  $\alpha$ ,  $\beta$ ,  $\lambda$ , and  $\eta$  are related to the reduced Planck's constant  $\hbar$  and effective masses by  $\alpha = \hbar^2/(2m_{cx})$ ,  $\beta = \hbar^2/(2m_{cy})$ ,  $\lambda = \hbar^2/(2m_{vx})$ , and  $\eta = \hbar^2/(2m_{vy})$ , respectively. The parameters  $\gamma_1 = \hbar v_1$  and  $\gamma_2 = \hbar v_2$  with  $v_1$  and  $v_2$  denoting the velocities along the x and y directions, respectively. These factors were obtained

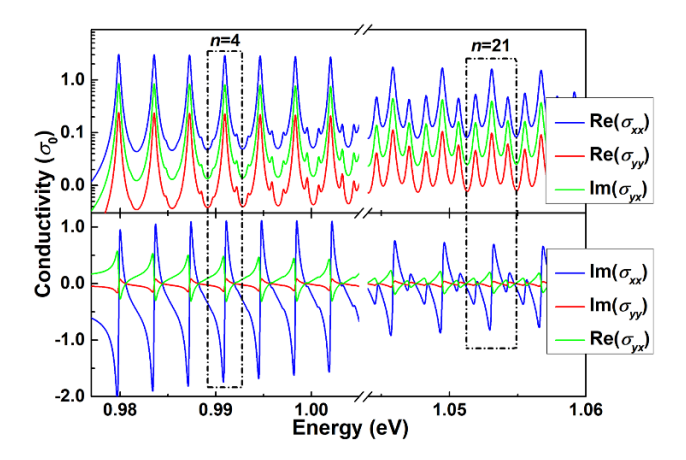


FIG. 2. Optical conductivity spectra of monolayer WTe<sub>2</sub> versus the  $\hbar\omega$  values at B=10 T. Oscillation periods at LL indexes n=4 and 21 are marked by two dashed-line boxes.

by fitting the first-principles band structures, and they are  $\alpha$ =11.25 eV·Å²,  $\beta$ =6.90 eV·Å²,  $\lambda$ =0.27 eV·Å²,  $\eta$ =1.08 eV·Å²,  $\gamma$ <sub>1</sub>=1.71 eV·Å, and  $\gamma$ <sub>2</sub>=0.48 eV·Å [22].

On the basis of a unitary transformation [21,22], the  $4\times4$  Hamiltonian  $H_{k\cdot p}$  in Eq. (1) can be separated into two decoupled  $2\times2$  Hamiltonian blocks corresponding to "spin-up" and "spin-down" states, respectively. These two  $2\times2$  blocks share the same dispersion relation. Thus, for brevity, we can only consider the spin-up Hamiltonian that reads [21,22]

$$H = \begin{pmatrix} E_c(k_x, k_y) & -iv_1 P_x - v_2 P_y \\ iv_1 P_x - v_2 P_y & E_v(k_x, k_y) \end{pmatrix},$$
(2)

where  $P_x = \hbar k_x$  and  $P_y = \hbar k_y$ .

To describe the PSHE in a general model, monolayer WTe<sub>2</sub> is assumed to be suspended in a free space where both the permittivities  $\varepsilon_1$  and  $\varepsilon_2$  of upper and bottom media are 1.0. One Gaussian wave packet with monochromatic frequency  $\omega$  impinges upon the surface of WTe<sub>2</sub> film with an incident angle  $\theta_i$ . The x and y axes of laboratory Cartesian coordinate (x, y, z) are along the armchair and zigzag orientations of WTe<sub>2</sub>, respectively, as sketched in Fig. 1(a). And a uniform static magnetic field  $\mathbf{B} = -B\hat{\mathbf{z}}$  is applied along the negative z axis. Within the linear-response theory [8,10], the magneto-optical response of monolayer WTe<sub>2</sub> is characterized by an optical conductivity tensor

$$\hat{\sigma}(\omega) = \begin{pmatrix} \sigma_{xx} & \sigma_{xy} \\ \sigma_{yx} & \sigma_{yy} \end{pmatrix}, \tag{3}$$

with

$$\sigma_{jk} = i\sigma_0 \frac{\hbar^2}{l_B^2} \sum_{n',n,c,v} \frac{\left[ f(E_{c,n'}) - f(E_{v,n}) \right] \left\langle c, n' \middle| v_j \middle| v, n \right\rangle \left\langle v, n \middle| v_k \middle| c, n' \right\rangle}{(E_{c,n'} - E_{v,n})(E_{c,n'} - E_{v,n} + \hbar\omega + i\Gamma)}, \quad (4)$$

where  $j, k \in \{x, y\}$ ,  $\sigma_{xy} = -\sigma_{yx}$  is Hall conductivity, n (or n') is the LL index of valence (or conduction) band,  $\sigma_0 = e^2/\pi \hbar$ ,  $l_B^2 = \hbar/(eB)$ ,  $f(E_{\zeta}) = \{ \exp[(E_{\zeta} - E_F)/k_B T] + 1 \}^{-1}$  is the Fermi-Dirac distribution function with Boltzman constant  $k_B$  and temperature T;  $E_{\nu,n}$  and  $E_{c,n'}$  are the LLs of valence and conduction bands, respectively; and  $v_{i/k}$  are the components of group velocities. The sum runs over all states  $|\zeta\rangle = |v,n\rangle$ and  $|\zeta'\rangle = |c,n'\rangle$  with  $\zeta \neq \zeta'$ . In this work, the level broadening factor  $\Gamma$  and temperature T are set to be 0.15 meV and 5 K, respectively. Besides, we take the Fermi energy  $E_F$ =0 such that the contribution from intraband transitions can be ignored [10,23]. Fig. 1(b) shows the LLs as a function of the magnetic field for the first 61 LLs in monolayer WTe<sub>2</sub>. More detailed introductions calculations of LLs and transition matrix elements  $v_{i/k}$  can be found from Eqs. (S1)-(S8) in [24].

According to the generalized 4×4 transfer-matrix formalism [25], the Fresnel reflection coefficients of free-suspended monolayer WTe<sub>2</sub> are calculated by

$$r_{pp} = -\frac{P_{12}^{--} S_{12}^{++} + \sigma_{xy} \sigma_{yx}}{P_{12}^{++} S_{12}^{+-} - \sigma_{xy} \sigma_{yx}},$$
 (5)

$$r_{sp} = -\frac{2\sigma_{xy}}{P_{12}^{++}S_{12}^{++} - \sigma_{xy}\sigma_{yx}},$$
 (6)

$$r_{ps} = \frac{2\sigma_{yx}}{P_{12}^{++}S_{12}^{+-} - \sigma_{xv}\sigma_{yx}},$$
 (7)

$$r_{ss} = \frac{P_{12}^{++} S_{12}^{--} + \sigma_{xy} \sigma_{yx}}{P_{12}^{++} S_{12}^{++} - \sigma_{xy} \sigma_{yx}},$$
(8)

with  $P_{12}^{\pm\pm} = 1/\cos\theta_i \pm 1/\cos\theta_i \pm \sigma_{xx}$  and  $S_{12}^{\pm\pm} = \cos\theta_i \pm \cos\theta_i \pm \sigma_{yy}$ . In the above Eqs. (5)-(8), all the conductivity tensor components are normalized to  $c\varepsilon_0/4\pi$  where c and  $\varepsilon_0$  stand for light velocity in vacuum and vacuum permittivity, respectively.

PSHE manifests itself as spin-dependent splitting, which appears in both transverse and in-plane directions. In the spin basis set, the linearly polarized state of light wave can be decomposed into two orthogonal spin components, i.e., the left- and right-circular polarization (LCP and RCP)

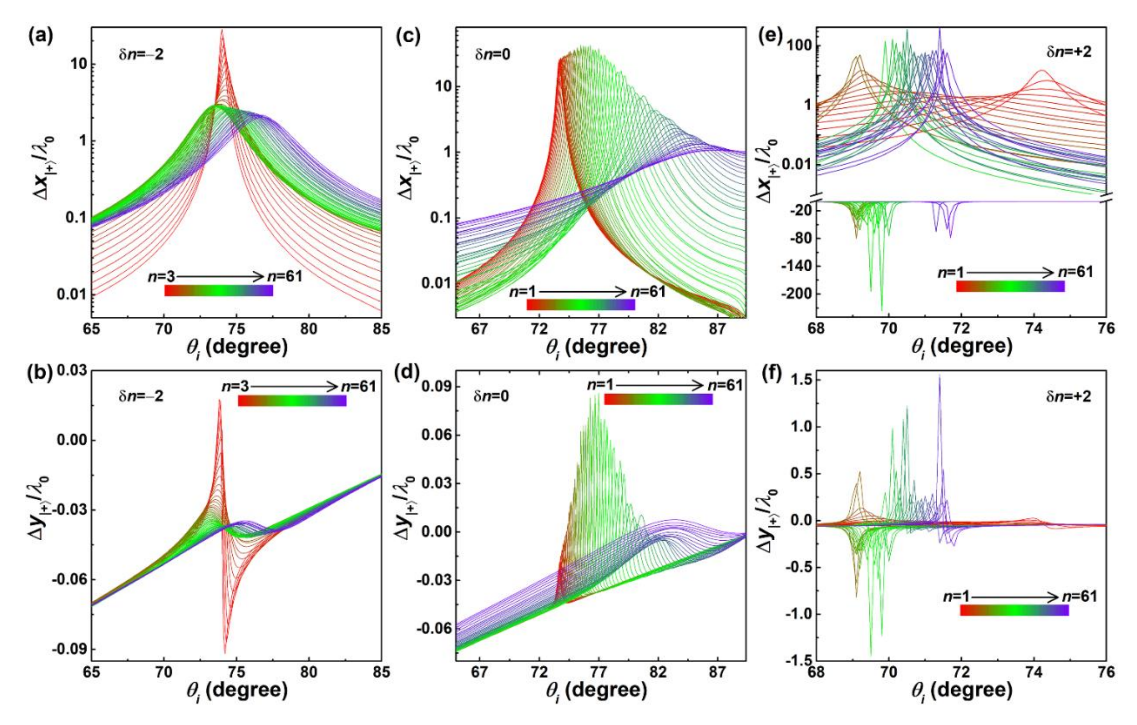


FIG. 3. (a)(c)(e) In-plane and (b)(d)(f) transverse spin-dependent shifts on the surface of monolayer WTe<sub>2</sub> versus the incident angle  $\theta_i$  and LL index n. (a)(b), (c)(d), and (e)(f) are for LL transitions  $\delta n = n' - n = -2$ , 0, and +2, respectively. The magnetic field B = 10 T.

components [10,26]. Under the paraxial approximation, photonic spin Hall shifts of these two orthogonal components in the reflected beam can be mathematically derived [26,27]. PSHE is sensitive to the polarization states of incident light. For simplicity, only *p*-polarized incident beam is considered in this paper. The corresponding inplane and transverse spin Hall shifts for LCP and RCP components, as indicated in Fig. 1(a), are derived from [10,26]

$$\Delta x_{|\pm\rangle} = \mp \frac{1}{k_0} \operatorname{Re} \left( \frac{r_{pp}}{r_{pp}^2 + r_{sp}^2} \frac{\partial r_{sp}}{\partial \theta_i} - \frac{r_{sp}}{r_{pp}^2 + r_{sp}^2} \frac{\partial r_{pp}}{\partial \theta_i} \right), \tag{9}$$

$$\Delta y_{|\pm\rangle} = \mp \frac{\cot \theta_i}{k_0} \operatorname{Re} \left( \frac{r_{pp} + r_{ss}}{r_{pp}^2 + r_{sp}^2} r_{pp} - \frac{r_{ps} - r_{sp}}{r_{pp}^2 + r_{sp}^2} r_{sp} \right), \tag{10}$$

respectively. Here,  $k_0 = 2\pi/\lambda_0$  is the wavevector in vacuum  $(\lambda_0 = 2\pi c/\omega)$  indicates the excitation wavelength), the superscripts  $|+\rangle$  and  $|-\rangle$  imply the LCP and RCP components, respectively. It is seen from the above equations that the inter-LL transitions can be used to modify the PSHE in virtue of their decisive impact on the conductivity tensor. Because  $\Delta x_{|+\rangle} = -\Delta x_{|-\rangle}$  and  $\Delta y_{|+\rangle} = -\Delta y_{|-\rangle}$ ,

we will only analyze the photonic spin Hall shifts for the LCP component in the following.

#### III. RESULTS AND DISCUSSIONS

Fig. 2 presents partially magnified  $\sigma_{xx}$ ,  $\sigma_{yy}$  and  $\sigma_{yx}$  spectra of monolayer WTe<sub>2</sub> at B=10 T. Their overall spectra ranging the  $\hbar\omega$  from 0.98 to 1.20 eV are given in Figs. S1-S3 in Ref. [24]. One can see that all the conductivity spectra are quantized and oscillated with increasing the photonic energy, and a three-peak structure is well resolved in each oscillation period in the real or imaginary part of  $\sigma_{xx}$  ( $\sigma_{yy}$ ) or  $\sigma_{yx}$ . By matching with LLs in Fig. 1(b), these three peaks from left to right correspond to interband transitions when the LL index changes  $\delta n = n' - n = -2$ , 0, and +2. In Fig. 2, oscillation periods at n=4 and 21 are marked by two dashed-line boxes, and interband transition rules are sketched in Fig. 1(c).

After substituting these LL-dependent conductivity components in Figs. 2 and S1-S3 into Eqs. (5)-(10), the optical spectra of photonic spin Hall shifts on the surface

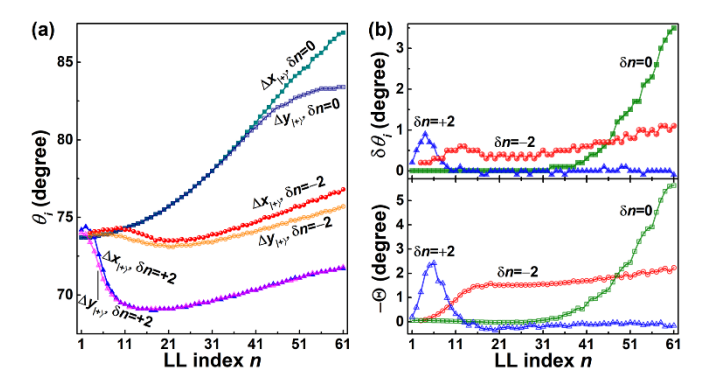


FIG. 4. (a) LL-dependent incident angles at which  $\Delta x_{|+\rangle}$  and  $\Delta y_{|+\rangle}$  have extremum displacements. (b) Upper subgraph: angle differences between incident angles of extremum displacements of  $\Delta x_{|+\rangle}$  and  $\Delta y_{|+\rangle}$ . Bottom subgraph: variations of the Hall angle  $-\Theta$  with respect to LLs. Symbols are the calculated values while solid lines are just drawn as a guide to the eye.

of monolayer WTe2 can be derived. Fig. 3 shows the variations of in-plane and transverse spin-dependent shifts with the incident angle  $\theta_i$  at increasing n from 1 (or 3) to 61 for  $\delta n = 0$ , +2 (or  $\delta n = -2$ ). To more clearly distinguish the curve shape, Fig. S4 illustrates the optical spectra of  $\Delta x_{(+)}$ inter-LL transitions and  $\Delta y_{|+\rangle}$ at  $|n=3\rangle \rightarrow |n'=1\rangle$  $|n=21\rangle \rightarrow |n'=21\rangle$ , and  $|n=55\rangle \rightarrow |n'=57\rangle$ . It is seen that the shift spectrum for each inter-LL transition gives a peak (it exhibits a dip for negative shifts). These peak or dip values correspond to their respective extremum displacements. Fig. 4(a) summarizes the  $\theta_i$  values of these extremum displacements. The extremum displacements of  $\Delta x_{|+\rangle}$  have a similar evolvement rule with that of  $\Delta y_{|+\rangle}$  at tunning LL index n, and the former is far larger than the latter. Thus, LL-dependent extremum displacements of  $\Delta x_{|+\rangle}$  and  $\Delta y_{|+\rangle}$  are summarized in Figs. 5 and S5, respectively. Besides, Figs. 5 and S5 also show the variations of conductivity differences  $Im(\sigma_{xx})-Im(\sigma_{yy})$  and  $Im(\sigma_{xx})-Re(\sigma_{yx})$  with LL index n. We find that the jagged spectra of conductivity differences are accompanied with slight quantum oscillations in the spectra of photonic spin Hall shifts.

For the case of  $\delta n = 0$ , it is seen from Fig. 4(a) that the peak position of  $\Delta x_{|+\rangle}$  (or  $\Delta y_{|+\rangle}$ ) gradually increases from 73.7° to 86.9°(or 83.4°) as the LL index *n* increases from 1

to 61. Extremum displacements of  $\Delta x_{|+\rangle}$  and  $\Delta y_{|+\rangle}$  appear at the same  $\theta_i$  value at  $n \leq 32$ , but they deviate from each other at n > 32 and their angle difference  $\delta \theta_i$  becomes larger and larger as the n increases [see upper subgraph in Fig. 4(b)]. Even if the slight quantum oscillation, the main variation trend of extremum displacements in Fig. 5(c) is that the displacements firstly increase and then decrease with an increment of the n. Especially, the in-plane spin-dependent shift  $\Delta x_{|+\rangle}$  gives the largest value of  $42.496\lambda_0$  at n = 21 [see Fig. 5(c)].

For the cases of  $\delta n=\pm 2$  [cf. Figs. 3(a)(b) and (e)(f)], their photonic spin Hall shifts have quite different LL-dependent behaviors, both of which are also different from that of  $\delta n=0$ . For example, the in-plane spin-dependent shift  $\Delta x_{|+\rangle}$  for  $\delta n=-2$  has the largest displacement of  $28.037\lambda_0$  at n=3 (n'=1), and it dramatically decreases to  $3.028\lambda_0$  as the n increases to 15 [see Fig. 5(b)]. By contrast, the  $\Delta x_{|+\rangle}$  for  $\delta n=+2$  gives the largest value of  $401.022\lambda_0$  at n=55, and its extremum displacements are strikingly oscillated with changing the n [see Fig. 5(d)]. The  $\theta_i$  values of extremum displacements for  $\delta n=0$ ,  $\pm 2$  also show completely different LL-dependent behaviors, as demonstrated in Fig. 4(a).

The variations of photonic spin Hall shifts with LLs could be attributed to LL-dependent Hall angle  $\Theta$ . Hall angle describes the efficiency of converting a longitudinal driving current into a lateral Hall current, which is calculated via  $\Theta = \arctan(\sigma_{yx}/\sigma_{xx})$  [28-30]. Fig. 4(b) shows that the variation tendency of angle difference  $\delta\theta_i$  is similar to that of  $-\Theta$  with changing the n. Extremum displacements of  $\Delta x_{|+\rangle}$  and  $\Delta y_{|+\rangle}$  appear at the same incident angle (i.e.,  $\delta\theta_i = 0$ ) when the  $\Theta$  is near to zero. If  $-\Theta$  is large enough, the angle difference  $\delta\theta_i \neq 0$  and it mainly increases with the increasing of  $-\Theta$ .

Fig. 5 shows that extremum displacements of PSHE are also impacted by Hall angle. For instance, at  $\delta n = 0$ , LL-dependent  $\Theta$  spectrum in Fig. 5(a) exhibits a wide peak around n = 21, matching with the peak position (n = 21) of LL-dependent  $\Delta x_{|+\rangle}$  spectrum in Fig. 5(c). At  $\delta n = -2$ , the  $\Theta$  is near to zero at n = 3 (n' = 1) and sharply decreases to  $-1.44^{\circ}$  as the n increases to 15, being in line with the curve

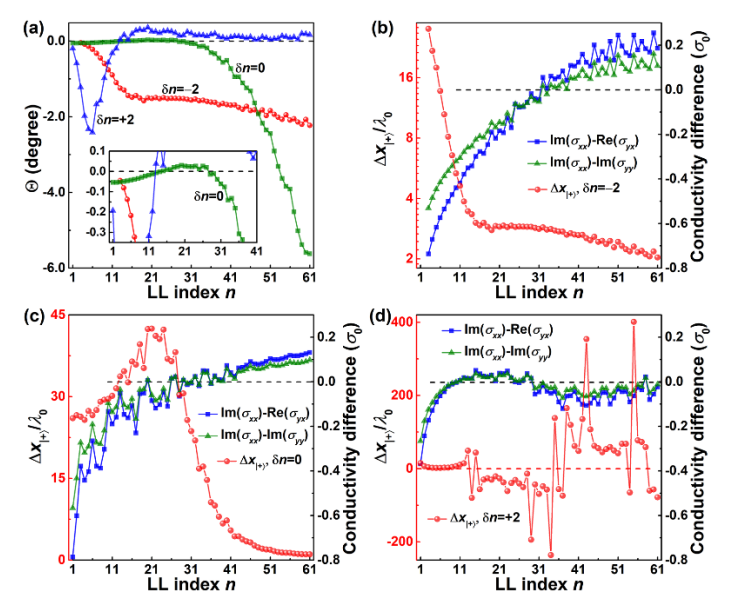


FIG. 5. (a) Variations of the Hall angle  $\Theta$  with respect to LLs. The inset shows partially magnified  $\Theta$  spectra for clarity. (b)-(d) Evaluations of the largest in-plane spin-dependent shifts with LL index n. (b), (c), and (d) are for the inter-LL transitions  $\delta n = -2$ , 0, +2, respectively. For comparison, LL-dependent conductivity differences  $\text{Im}(\sigma_{xx})-\text{Im}(\sigma_{yy})$  and  $\text{Im}(\sigma_{xx})-\text{Re}(\sigma_{yx})$  are also shown in (b)-(d). The graduation lines at which the vertical coordinate axis equals zero are marked by dashed horizontal lines. Symbols are the calculated values while solid lines are just drawn as a guide to the eye. The magnetic field B = 10 T.

shape of  $\Delta x_{|+\rangle}$  spectrum in Fig. 5(b). At  $\delta n = +2$ , both the  $\Theta$  and  $\Delta x_{|+\rangle}$  spectra in the range  $1 \le n \le 12$  exhibits a dip [cf. Figs. 5(a) and (d)], and the largest displacement of  $\Delta x_{|+\rangle}$  is only 14.927 $\lambda_0$  in this range. In contrast, the  $\Theta$  oscillates near  $0^{\circ}$  at  $n \ge 13$  such that the  $\Delta x_{|+\rangle}$  also strikingly oscillates and gives relatively larger displacements (the largest displacement  $401.022\lambda_0$  appears at n = 55 with  $\Theta = 0.11^{\circ}$ ).

According to Figs. 5 and S5, we construct an empirical formula between photonic spin Hall shifts with Hall angle by

$$F(\Theta) = \sum_{i=1}^{5} a_i \exp \left[ -\left(\frac{\Theta - b_i}{c_i}\right)^2 \right]. \tag{11}$$

In the above equation,  $F(\Theta)$  can be either the in-plane or transverse spin Hall shift, the factors  $a_i$ ,  $b_i$ , and  $c_i$  are coefficients and their detailed values are listed in Table S1

[24]. Fig. S6 presents the extremum displacements of  $\Delta x_{|+\rangle}$  and  $\Delta y_{|+\rangle}$  as a function of Hall angle  $\Theta$ . It is found that  $F(\Theta)$  is in accordance with the variation tendency of  $\Delta x_{|+\rangle}$  and  $\Delta y_{|+\rangle}$  calculated via Eqs. (9) and (10).

On the basis of the above discussions, it could be concluded that a very small Hall angle results in greatly enhanced PSHE. Even so, Hall angle can not be zero if we want to obtain a giant PSHE. This is because that the Hall conductivity  $\sigma_{xy} = 0$  will lead to  $r_{sp} = r_{ps} = 0$  according to Eqs. (6) and (7). In consequence, the  $\Delta x_{|+\rangle}$  will equal to zero and the  $\Delta y_{|+\rangle}$  will become far smaller than excitation wavelength  $\lambda_0$  based on Eqs. (9) and (10). This idea is further evidenced by modulating the magnetic induction intensity B.

Figs. 6(a) and S7 show the changes of complex optical conductivities of monolayer WTe2 with the B values at LL index n = 21. Accordingly, magnetic-field-dependent Hall angle and photonic spin Hall shifts can be derived, as shown in Figs. 6(b) and (c), respectively. For LL transitions  $\delta n = -2$  and 0, both of their Hall angles are gradually decreased with increasing the B value. Thereby, extremum displacements of  $\Delta x_{\perp}$  and  $\Delta y_{\perp}$  are also gradually decreased with enhancing the magnetic field. Because the  $\Theta$  values of  $\delta n = -2$  are far away from 0°, the  $\Delta x_{|+\rangle}$  (or  $\Delta y_{|+\rangle}$ ) of  $\delta n = -2$ is far smaller than that of  $\delta n = 0$  [cf. red and green symbols in Fig. 6(c)]. For the LL transition  $\delta n = +2$ , the optical spectra of conductivity components  $Im(\sigma_{xx})$ ,  $Im(\sigma_{yy})$ , and  $Re(\sigma_{xy})$  cross around the coordinate  $(0\sigma_0, 8 \text{ T})$ , as shown by blue symbols in Fig. 6(a). As a result, photonic spin Hall shifts  $\Delta x_{|+\rangle}$  and  $\Delta y_{|+\rangle}$  of  $\delta n = +2$  in Fig. 6(c) change from positive to negative values as the B increases from 8 T to be  $\geq 9$  T. As the B increases from 5 T to 8 T, the  $\Theta$ increases from -0.06° to 0.12°, correspondingly, the extremum displacement of  $\Delta x_{|+\rangle}$  (or  $\Delta y_{|+\rangle}$ ) gradually increases from  $25.817\lambda_0$  to  $271.683\lambda_0$  (or from  $0.003\lambda_0$  to 1.002 $\lambda_0$ ). At  $B \ge 9$  T, the  $\Theta$  gradually deviates from  $0^{\circ}$  as the B increases, thus, the in-plane and transverse displacements (i.e.,  $|\Delta x_{|+\rangle}|$  and  $|\Delta y_{|+\rangle}|$ ) gradually decrease with enhancing the magnetic field.

Fig. 6(d) exhibits magnetic-field-dependent  $\theta_i$  values at which  $\Delta x_{|+\rangle}$  and  $\Delta y_{|+\rangle}$  have extremum displacements. Because

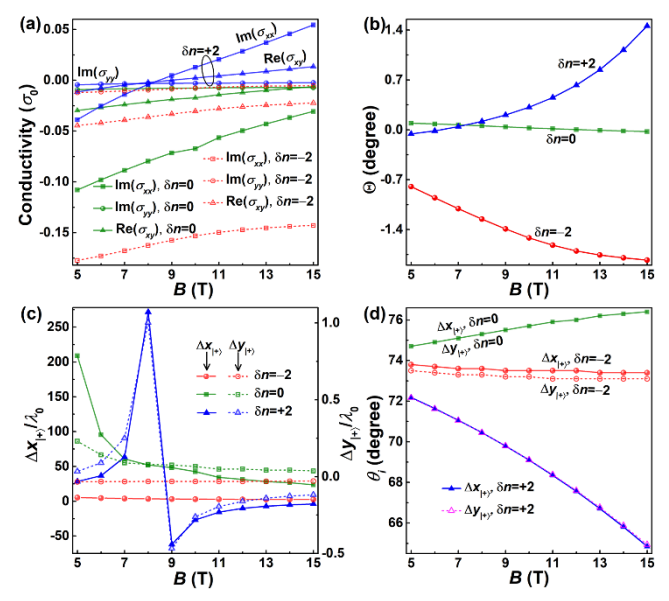


FIG. 6. At the transitions  $\delta n=0,\pm 2$  with n=21, (a) complex optical conductivities versus the magnetic induction intensity B; (b) variations of the Hall angle  $\Theta$  with respect to the B; (c) extremum displacements of  $\Delta x_{|+\rangle}$  (solid symbols, refer to left vertical axis) and  $\Delta y_{|+\rangle}$  (open symbols, refer to right vertical axis) versus the B; (d) magnetic-field-dependent incident angles at which  $\Delta x_{|+\rangle}$  and  $\Delta y_{|+\rangle}$  have the extremum displacements. Symbols are the calculated values while solid or dashed lines are just drawn as a guide to the eye.

Hall angles are close to  $0^{\circ}$  (or far away from  $0^{\circ}$ ) at  $\delta n = 0$  (or  $\delta n = -2$ ),  $\Delta x_{|+\rangle}$  and  $\Delta y_{|+\rangle}$  present their respective extremum displacements at the same (or different) incident angles, as marked by green (or red) symbols in Fig. 6(d). For the transition  $\delta n = +2$ , extremum displacements of  $\Delta x_{|+\rangle}$  and  $\Delta y_{|+\rangle}$  appear at nearly the same incident angle at  $B \le 12$  T. When the magnetic field is  $B \ge 13$  T, Hall angles of  $\delta n = +2$  become larger than  $0.7^{\circ}$  such that the incident angle of extremum displacement of  $\Delta y_{|+\rangle}$  begins to deviate from that of  $\Delta x_{|+\rangle}$ , as marked by open and solid triangle symbols in Fig. 6(d).

Finally, we also calculate the photonic spin Hall shifts on the surface of monolayer WTe<sub>2</sub> without the external magnetic field. At this condition, Hall conductivity  $\sigma_{xy}$  equals to zero, longitudinal and transverse optical conductivities of monolayer WTe<sub>2</sub> are calculated by the

Lorentz-Drude model [31]. Fig. S8 shows the optical conductivity spectra of WTe<sub>2</sub> at B=0 T. Corresponding photonic spin Hall shifts, as a function of the photonic energy and the incident angle, are shown in Fig. S9. Results show that all the photonic spin Hall shifts are smaller than  $0.15\lambda_0$ . Therefore, a non-vanishing Hall conductivity together with near-zero Hall angle is responsible for the aforementioned giant PSHE.

### IV. CONCLUSIONS

To summarize, LL-engineered PSHE has been studied in monolayer WTe2. Results show that PSHE induced via LL transitions  $\delta n = 0, \pm 2$  in WTe<sub>2</sub> exhibit completely different dependent behaviors on LL index. For  $\delta n = 0$ , the extremum displacements of PSHE mainly increase with increasing LL index up to n = 21 and decreases thereafter. For  $\delta n = -2$ , photonic spin Hall shifts decrease sharply as n increases to 15, and then tend to slow variations. For  $\delta n =$ +2, the extremum displacement is strikingly oscillated with changing the n and it gives the largest value (more than 400 times of the incident wavelength) at n = 55. PSHE induced via LL transitions  $\delta n = 0, \pm 2$  also present different physical responses at tuning the incident angle of incident and magnetic induction intensity. These photons discrepancies are attributed to Hall-conductivity-incurred Hall angle  $\Theta$  because the variation tendency of extremum displacements of PSHE is similar to that of  $\Theta$  with changing the LL index. Remarkably enhanced PSHE occurs at near-zero Hall angles. In-plane and transverse extremum displacements appear at different incident angles when the value of  $|\Theta|$  is large enough, and their incidentangle deviation becomes larger and larger with the increasing of  $-\Theta$ . These results provide insight into the fundamental properties of spin-orbit interaction of light in time-reversal symmetry breaking 2D quantum systems. They may also open up new possibilities for integrating quantum Hall physics with spin-photon interactions, facilitating the development of novel quantum photonic devices.

## ACKNOWLEDGMENTS

The author G. Jia acknowledges the financial support by National Natural Science Foundation of China (Grant No. 11804251). The author X. Zhou acknowledges the financial

support by National Natural Science Foundation of China (Grant Nos. 12374273, 12421005) and Hunan Provincial Major Sci-Tech Program (Grant No. 2023ZJ1010).

- [1] S. Liu, I. A. Malik, V. L. Zhang and T. Yu, Lightning the spin: harnessing the potential of 2D magnets in opto-spintronics, Adv. Mater. 37, 2306920 (2025).
- [2] J. K. König, J. M. Fitzgerald and E. Malic, Magnetooptics of anisotropic exciton polaritons in twodimensional perovskites, Nano Lett. 25, 8519-8526 (2025).
- [3] B. Göbel and I. Mertig, Orbital Hall effect accompanying quantum Hall effect: Landau levels cause orbital polarized edge currents, Phys. Rev. Lett. 133, 146301 (2024).
- [4] X. Y. Zhou, W. Chen and X. Z. Zhu, Anisotropic magneto-optical absorption and linear dichroism in two-dimensional semi-Dirac electron systems, Phys. Rev. B 104, 235403 (2021).
- [5] N. M. Wei, G. P. Xu, I. S. Villadiego and C. L. Huang, Landau-level mixing and SU(4) symmetry breaking in graphene, Phys. Rev. Lett. 134, 046501 (2025).
- [6] T. Fujii, Y. Nakai, M. Hirata, Y. Hasegawa, Y. Akahama, K. Ueda and T. Mito, Giant density of states enhancement driven by a zero-mode Landau level in semimetallic black phosphorus under pressure, Phys. Rev Lett. 130, 076401 (2023).
- [7] Y. M. Shao, S. Moon, A. N. Rudenko, J. Wang, J. Herzog-Arbeitman, M. Ozerov, D. Graf, Z. Y. Sun, R. Queiroz, S. H. Lee, Y. L. Zhu, Z. Q. Mao, M. I. Katsnelson, B. A. Bernevig, D. Smirnov, A. J. Millis and D. N. Basov, Semi-Dirac Fermions in a topological metal, Phys. Rev. X 14, 041057 (2024).
- [8] W. Chen, X. Y. Zhou, W. K. Lou and K. Chang, Magneto-optical conductivity and circular dichroism in *d*-wave altermagnets, Phys. Rev. B 111, 064428 (2025).
- [9] T. Jiang, Y. T. Shu, Y. F. Song, Y. Zhang, Z. X. Wen and Z. M. Luo, Active manipulation of the plasmonic induced asymmetric photonic spin Hall effect, J. Phys.

- D-Appl. Phys. 57, 255104 (2024).
- [10] G. Y. Jia, G. Li, Y. Zhou, X. L. Miao and X. Y. Zhou, Landau quantisation of photonic spin Hall effect in monolayer black phosphorus, Nanophotonics 9, 225-233 (2020).
- [11] T. T. Tang, J. Li, L. Luo, P. Sun and J. Q. Yao, Magneto-optical modulation of photonic spin Hall effect of graphene in terahertz region, Adv. Opt. Mater. 6, 1701212 (2018).
- [12] X. L. Xie, H. D. Cheng, H. F. Chen, H. D. Zheng, Y. C. Zhong, J. Y. Tang, J. H. Yu, Z. Chen and W. G. Zhu, Photonic spin Hall effect by electro-optically induced Pancharatnam-Berry phases, Phys. Rev. Lett. 134, 113805 (2025).
- [13] G. Wan, Z. H. Ma, Y. Xue, C. Zhang, Y. Chen and X. X. Zhou, Photonic spin Hall effect at an optical bound state in the continuum, Phys. Rev. B 111, 085411 (2025).
- [14] Y. Fernández-Méndez, R. Carrillo-Bastos and J. A. Maytorena, Probing quantum geometric capacitance via photonic spin Hall effect, Phys. Rev. B 112, L121407 (2025).
- [15] B. Wang, K. X. Rong, E. Maguid, V. Kleiner and E. Hasman, Probing nanoscale fluctuation of ferromagnetic meta-atoms with a stochastic photonic spin Hall effect, Nat. Nanotech. 15, 450-456 (2020).
- [16] M. Abbas, G. Din, H. R. Hamedi and P. Zhang, Manipulation of the photonic spin Hall effect in a cavity magnomechanical system, Phys. Rev. A 111, 053716 (2025).
- [17] T. T. Tang, K. Shen, Y. J. Tang, J. Li, Y. He, X. Liang, C. Y. Li, J. Shen and L. Luo, Photonic spin Hall effect under the action of a full-angle three-dimensional magnetic field in space, Appl. Phys. Lett. 124, 151104 (2024).
- [18] L. Cai, M. X. Liu, S. Z. Chen, Y. C. Liu, W. X. Shu,

- H. L. Luo and S. C. Wen, Quantized photonic spin Hall effect in graphene, Phys. Rev. A **95**, 013809 (2017).
- [19] M. Shah and M. S. Anwar, Valley and spin polarized quantized spin dependent photonic shifts in topological silicene, Phys. Lett. A 401, 127342 (2021).
- [20] X. F. Qian, J. W. Liu, L. Fu and J. Li, Quantum spin Hall effect in two-dimensional transition metal dichalcogenides, Science 346, 1344-1347 (2014).
- [21] D. L. Wang, A. Q. Hu, J. P. Lv and G. J. Jin, Electric field modulated valley- and spin-dependent electron retroreflection and Klein tunneling in a tilted n-p-n junction of monolayer 1T'-MoS<sub>2</sub>, Phys. Rev. B **107**, 035301 (2023).
- [22] L. K. Shi and J. C. W. Song, Symmetry, spin-texture, and tunable quantum geometry in a WTe<sub>2</sub> monolayer, Phys. Rev. B **99**, 035403 (2019).
- [23] X. Y. Zhou, W. K. Lou, F. Zhai and K. Chang, Anomalous magneto-optical response of black phosphorus thin films, Phys. Rev. B 92, 165405 (2015).
- [24] See Supplemental Material at <a href="http://link.aps.org/supplemental/10.1103/PhysRevB.XXXXX">http://link.aps.org/supplemental/10.1103/PhysRevB.XXXXX</a> for calculations on LLs and transition matrix elements; variations of in-plane and transverse spin-dependent shifts with Hall angles; PSHE without the external magnetic field; table S1 and Figs. S1-S9.
- [25] O. V. Kotov and Y. E. Lozovik, Hyperbolic hybrid waves and optical topological transitions in few-layer anisotropic metasurfaces, Phys. Rev. B 100, 165424 (2019).
- [26] G. Y. Jia, Z. X. Huang, Q. Y. Ma and G. Li, Photonic spin Hall effect on the surfaces of type-I and type-II Weyl semimetals, Nanophotonics 9, 715-723 (2020).
- [27] L. G. Xie, Q. S. Liu, H. Dou, Z. X. Li and X. X. Zhou, Quantitative relationship between in-plane and outof-plane photonic spin Hall effects in vortex beams, Phys. Rev. B 112, 075402 (2025).
- [28] P. G. Li, J. Koo, W. Ning, J. G. Li, L. X. Miao, L. J. Min, Y. L. Zhu, Y. Wang, N. Alem, C. X. Liu, Z. Q. Mao and B. H. Yan, Giant room temperature

- anomalous Hall effect and tunable topology in a ferromagnetic topological semimetal Co<sub>2</sub>MnAl, Nat. Commun. 11, 3476 (2020).
- [29] S. H. Zhang, D. F. Shao, Z. A. Wang, J. Yang, W. Yang and E. Y. Tsymbal, Tunneling valley Hall effect driven by tilted Dirac Fermions, Phys. Rev. Lett. 131, 246301 (2023).
- [30] J. J. Feng, C. Xiao, Y. Gao and Q. Niu, Magnetic field influenced electron-impurity scattering and magnetotransport, Phys. Rev. B 100, 134202 (2019).
- [31] C. Wang, S. Y. Huang, Q. X. Xing, Y. G. Xie, C. Y. Song, F. J. Wang and H. G. Yan, Van der Waals thin films of WTe<sub>2</sub> for natural hyperbolic plasmonic surfaces, Nat. Commun. 11, 1158 (2020).